

Article

Predicting Ceramic Wool Diameter by Motor Frequency Using Improved BP Neural Network

Tengzhou Xu, Jie Huang, Yang Li and Tao Chen *

College of Aeronautical Engineering, Nanjing Vocational University of Industry Technology,
Nanjing 210023, China

* Correspondence: taochen@niit.edu.cn

Abstract: Ceramic wool was prepared by the melt-spinning method, and the diameter was the main factor severely affecting the performance of the final product which was difficult to check online. The current study discusses the approximate simulation of the fiber formation and presents a fast precision measuring method to predict the ceramic wool diameter using an improved Back-Propagation (BP) neural network. Particle Swarm Optimizer (PSO) was employed to optimize the neural network structure for its presentation of the relationship between the motor frequency of the spinning wheel and the ceramic wool diameter. The superiority of this method was demonstrated by experiment compared with the least square method (LSM). The mean measurement error of PSO-BP was 0.471%, which was lower than that of LSM. The presented PSO-BP method was very valuable for predicting the wool diameter, and the neural networks could solve nonlinear problems successfully, which was certified by the actual prediction of ceramic wool diameter.

Keywords: ceramic wool diameter; motor frequency; PSO-BP; wool diameter prediction

1. Introduction

Energy was what was keeping our head above water and allowing us to continue to grow. However, the over-consumption of energy and intensive exploitation of natural resources had raised the global concern [1–3]. Therefore, any effective power-saving technology that assisted efforts to reduce energy consumption was an advisable trend to be followed. In China, slag and mineral wool products had a glorious prospect as the government and communities increasingly had their eye on the fire safety of high-rise buildings [4,5]. Ceramic wool, a kind of classification of mineral wool, is an inorganic insulation material and was primarily designed for advanced fire prevention applications [6,7]. Undoubtedly, ceramic wool felt with low moisture absorption, light weight, low thermal conductivity, and non-combustible property was expected to provide a new solution in the fields of industrial, automotive, aerospace, and medical engineering applications under extreme environmental conditions [8–11]. The common production process of ceramic wool mainly includes two steps: melting and fiber forming. In this method, an ideal highly viscous fluid is formed in the blast furnace with the temperature range of 1823 K to 1973 K and then falls on a spinning wheel with a rotating speed nearly 8000–1000 rpm. Due to the centrifugal force, the fluid is dragged into filaments. The viscosity increases rapidly, and the instability diminishes notably as the string increases in length. A higher temperature blast furnace was invented to produce ceramic wool directly which not only reduced energy consumption but also resulted in a better use of waste energy [12–14]. Clearly, the ceramic wool felt was prepared by a random distribution of ceramic wool. With the gradual implementation of China's 2025 plan, finer primary wool diameter which dramatically affected the product performance was required for higher quality products with non-combustible property and low thermal conductivity.

Many researchers have attached importance to the production process. Zhao et al. developed a novel kinematic model for molten slag fiberization, especially on the diameter



Citation: Xu, T.; Huang, J.; Li, Y.; Chen, T. Predicting Ceramic Wool Diameter by Motor Frequency Using Improved BP Neural Network. *Appl. Sci.* **2023**, *13*, 226. <https://doi.org/10.3390/app13010226>

Academic Editor: Rocco Furferi

Received: 30 November 2022

Revised: 14 December 2022

Accepted: 22 December 2022

Published: 24 December 2022



Copyright: © 2022 by the authors. Licensee MDPI, Basel, Switzerland. This article is an open access article distributed under the terms and conditions of the Creative Commons Attribution (CC BY) license (<https://creativecommons.org/licenses/by/4.0/>).

and length of slag fiber to predict slag fiber properties [15]. Under given process parameters and relevant hypotheses, the prediction model was established which indicated that the slag viscosity and the rotational speed of spinning wheel had a great effect on the fiber dimensions systematically. Bajcar et al. presented a computer-aided visualization method to study the distribution of mineral wool fiber and a numerical model was used to confirm the relationship of the local aerodynamic characteristic of the airflow and mineral wool thickness [16]. Gerogiorgis et al. focused on the molten slag fiber generation stochastic modeling and studied the fiber flight trajectory differences under different operating conditions [17]. The strong industrial potential of molten slag fiberization was proved. Chelikani and Sparrow devoted all energies to the Coanda effect on the trajectory of fine fibers in production which was discussed under different standoff distances by means of numerical simulation [18]. Hocevar presented a regression model in the mineral wool production processes which was provided for automated control [19]. Although fibers with different physical characteristics could be empirically produced, the specific process of the melt fiberization remained unclear.

The speed of the spinning rotating wheel which was difficult to indicate played a decisive role in the fiber diameters. However, there was no precise theory to explain or predict the mechanical process of the filament formation. Moreover, the ceramic wool diameter could not be effectively obtained directly either which resulted in mismatch risks. The motor frequency of the spinning wheel was always detected to show the rotating speed in the real production. However, unfortunately, there were only a few reports about the ceramic wool production process between the motor frequency of the spinning wheel and the ceramic wool diameter. In this article, the approximate simulation of the fiber formation is discussed. Furthermore, a novel method called improved BP neural networks with training data is utilized to predict the relationship between the motor frequency and the ceramic wool diameter. PSO is presented to optimize the neural network structure and the measuring precision is calculated. Compared with the Least Square Method (LSM), the superiority of this method is verified. The results reveal that the PSO-BP neural network could accurately predict the wool diameter with less error.

2. Preparation of the Ceramic Wool

Raw materials such as bauxite and coal gangue for ceramic wool production were smashed, mixed, and melt together. Then, the homogeneous mixed melted viscous fluid fell on the roller surface. Then, it was sucked into the moving centrifuge disc due to its own viscosity. On the disc surface, a layer of melt film formed gradually and the film was dragged into filaments due to the centrifugal force. The viscosity increased rapidly, and the instability diminished notably as the string increased in length, which allowed the wool to grow. The actual forming process and schematic diagram of the ceramic wool on the rotating wheel is shown in Figure 1.

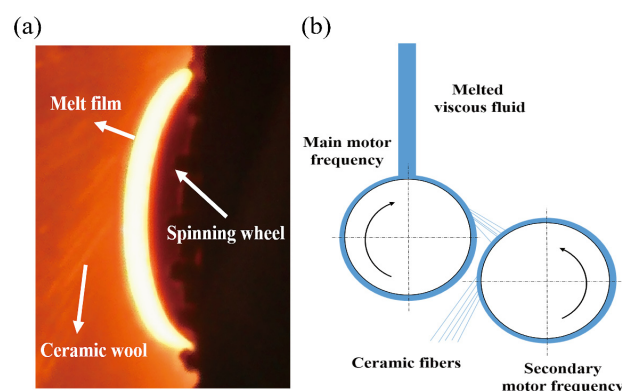


Figure 1. (a) The actual forming process of the ceramic wool on the rotating wheel; (b) The schematic diagram of the process.

Rotating speed had a great influence on the ceramic wool diameter. However, it was not mature to describe the process by numerical simulation while studying the practical problems of centrifugal wool formation. As the complex fluid resulted from many influencing factors, the simulation results differ greatly from the actual results [20–22]. In addition, in the real production process, high rotating speed resulted in grossly increased instabilities under the high temperature environment. Moreover, the viscous fluid continued to flow to another spinning disc accompanying the action of collision and centrifugation. In fact, the fiber forming process mostly occurred in the main centrifuge disc. To facilitate the discussion of the centrifugation wool formation mechanism, the fiberization process on the main motor frequency was mainly studied and the secondary motor frequency was fixed in this paper.

A similar simulation method was used to analyze the ceramic wool formation process. Meanwhile, the following assumptions were made for the particle force analysis of liquid melt in the centrifugal process:

- (1) The temperature of the viscous fluid was constant when falling from the directing channel onto the spinning machine;
- (2) The viscosity of the viscous fluid was not changed in the fiber forming process;
- (3) The viscous fluid possessed constant density for its incompressibility;
- (4) The influence of severe temperature and complex physicochemical on the viscous fluid properties was ignored;
- (5) The ceramic wool fibers were thrown out along the tangent of the separation point of the roll surface.

Figure 2 illustrates a simplified process of the ceramic wool fiberization. Firstly, the fixed viscous fluid fell downward onto the spinning wheel as shown in the Figure 2a. For an instant, the fluid turned into a thin melt film due to the centrifugal force. The supposed droplets were formed on the wheel as the surface tension increased [23]. The initial speed of the droplet was the same as the roller speed and the droplet velocity direction tended to be parallel to the tangent direction of the roller surface which was also the ideal direction of the droplet elongation. Then, the droplet was stretched into the filament as shown in Figure 2b,c [24]. In a very short time, the elongation process ended and the length of the filament was almost equal to the displacement distance of the droplet. Based on the conservation of mass, the fiber diameter decreased as the length increased. However, the length depended on the initial speed which was related to the main motor frequency. It indicated that the main motor frequency indeed played a decisive role in the fiber diameter [25].

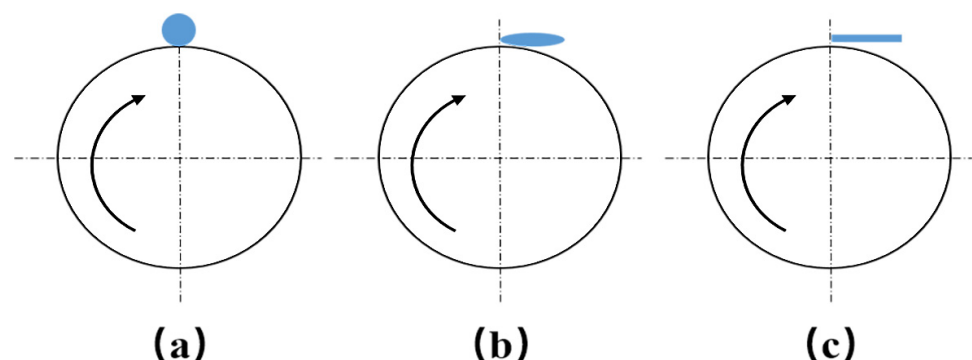


Figure 2. Planar diagram of the simplified fiberization process: (a) The moment of the fixed viscous fluid falling downward onto the spinning wheel; (b) Droplet stretch stage; (c) Droplet final filament stage.

3. Experimental Procedure

In this experimental part, the main raw materials with additives (mainly Al_2O_3 and SiO_2) were used to prepare the ceramic wool. To predict the relationship between the main

motor frequency and the ceramic wool diameter, different samples were prepared with the main motor frequencies ranging from 220.9 to 378.5 Hz which was in the certain frequency range of the real produce process. The corresponding relationship between the frequency and rotation speed of the main motor is 1 Hz for 30 rad/min, the wheel rotation speed range is between 6627 rad/min and 11625 rad/min. The mixture could not be rolled into wool when the main motor rotation speed was too low. However, at high frequency, the mechanical vibrations were inevitable which affected the fiber quality.

The diameters were tested according to the standard procedure of GBT7690.5-2001 while the histogram and normal distribution curves were drawn according to the data observed by VOM.100 points. Figures 3 and 4 show the SEM images of the ceramic fibers with different diameters with the specified main motor frequency. The values of the diameters varied from 1.058 μm to 4.538 μm , which verified that the ceramic fibers were discrete. Hence, to obtain the mean ceramic wool diameter, Figure 5 illustrated the diameter distribution of 100 ceramic fibers with the main motor frequency of 280.0 Hz. As shown in the picture, 100 squares with different colors matched 100 values and the white square represents the highest value. It indicated that the fiber diameters ranged from 1.950 to 5.210 μm in the same sample. The mean ceramic wool diameter was 3.524 μm . However, the diameters of the ceramic fiber fluctuated greatly in the actual production. To improve the results accuracy, five samples were collected at a constant frequency, and the final data with ten different motor frequencies are shown in Table 1.

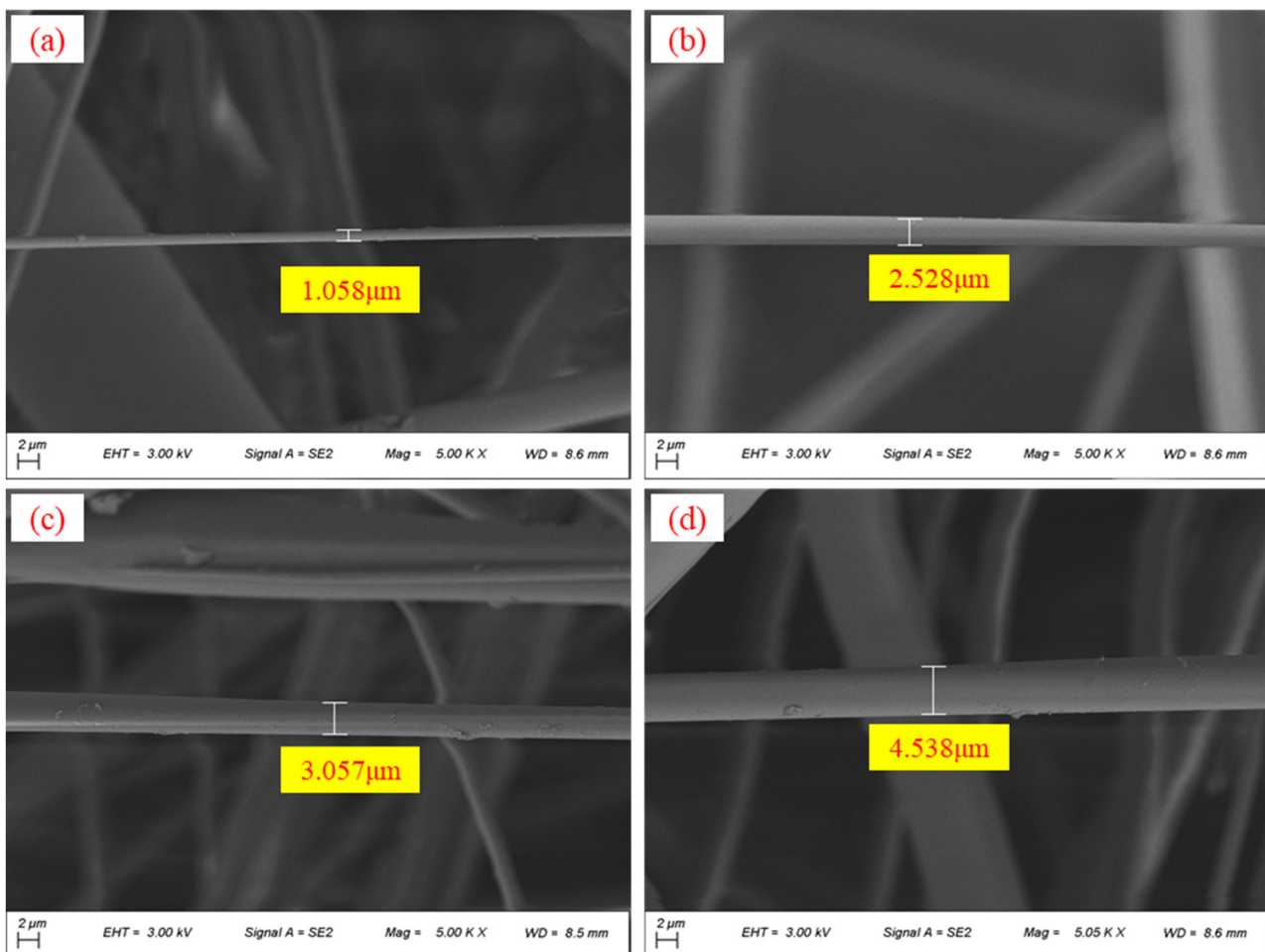


Figure 3. SEM images of ceramic fibers with different diameters.

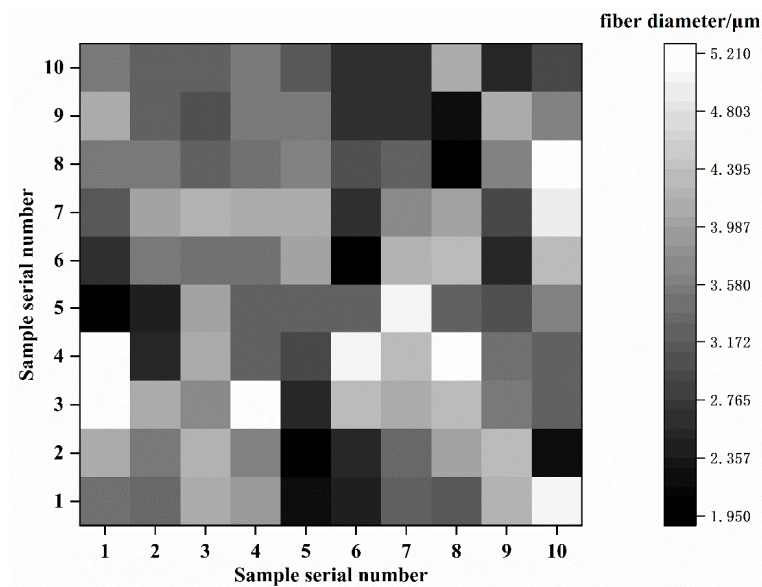


Figure 4. Diameter distribution of 100 ceramic fibers.

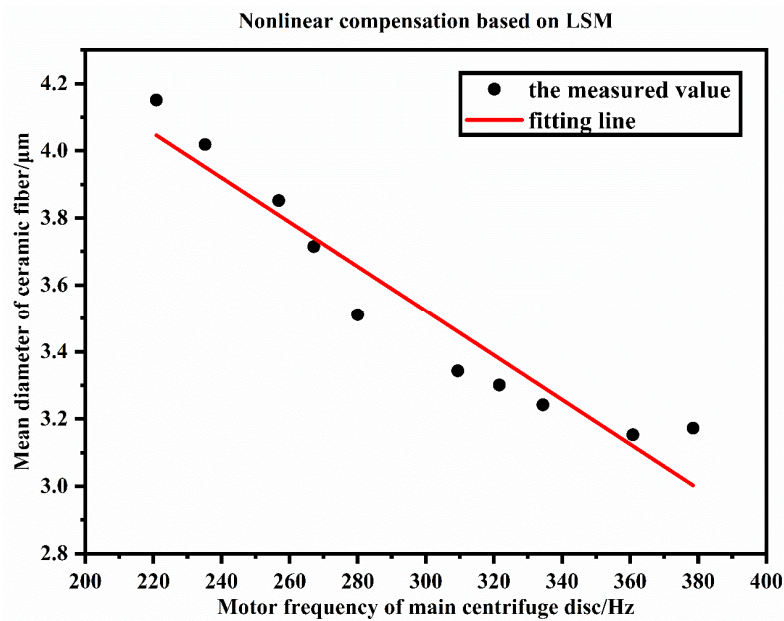


Figure 5. Nonlinear compensation model based on LSM.

Table 1. The Mean Fiber Diameter Date with Ten Different Main Motor Frequencies.

The Main Motor Frequency/Hz	The Mean Diameter of Each Sample/ μm					The Mean Ceramic Wool Diameter/ μm
	1	2	3	4	5	
220.9	4.154	4.158	4.135	4.152	4.156	4.151
235.2	4.023	4.025	3.994	4.031	4.024	4.019
256.8	3.851	3.859	3.812	3.867	3.869	3.852
267.1	3.731	3.719	3.687	3.721	3.716	3.715
280.0	3.524	3.519	3.489	3.513	3.511	3.511
309.4	3.347	3.345	3.337	3.342	3.343	3.343
321.6	3.309	3.313	3.267	3.305	3.310	3.301
334.4	3.252	3.245	3.226	3.243	3.245	3.242
360.8	3.158	3.156	3.148	3.152	3.15	3.153
378.5	3.176	3.181	3.160	3.172	3.174	3.173

4. The Calibration of Measurement Model

In order to get higher precision measurement, the accuracy of the model calibration should be examined. Firstly, the frequency of the secondary motor was fixed and that of the main motor frequency was changed according to the pre-set value. The ceramic wool samples were cut while the running of production process was stable and reliable. The fiber diameters were measured in accordance with the standard procedure. Ten different main motor frequencies were selected for testing experiments. Based on the testing results, the relationship between the main motor frequency and the characteristic value of the mean ceramic diameter was fitted by LSM and PSO-BP neural networks, respectively, in the following sections.

4.1. LSM Model

LSM is a mathematical optimization technique. It has been broadly used in the engineering application to minimize the squared error and find the best matched functions for the data. The anticipated data could be easily calculated by the LSM, and the sum of squared errors between the actual data and the obtained data could be obtained. Based on its simple characteristics, no statistical parameters were required [26].

For error calculation, the motor frequency was set to be x as the input layer and the corresponding mean ceramic diameter was set to be y_i as the output layer, a series of paired data $(x_1, y_1), (x_2, y_2) \dots (x_m, y_m)$ was obtained. These points were assumed to near a line, the equation of this line could be set as

$$y_i = a_0 + a_1x, \quad (1)$$

where a_0 and a_1 were the required determined parameters, respectively.

To estimate the constants, the optimization criterion was defined as the minimum of the sum of squares between the measured value Y and the calculated value Y_j where

$$Y_j = a_0 + a_1X_i, \quad (2)$$

Suppose the optimization criterion was

$$Z = \sum(Y_i - Y_j)^2 = \sum(Y_i - a_0 - a_1X_i)^2, \quad (3)$$

In order to get the minimum value of Z , the partial derivatives for a_0 and a_1 of Z were calculated and set to zero. The equations were

$$\sum 2(Y_i - a_0 - a_1X_i) = 0, \quad (4)$$

$$\sum 2(Y_i - a_0 - a_1X_i)X_i = 0, \quad (5)$$

The parameters a_0 and a_1 were:

$$a_0 = \frac{\sum Y_i - a_1 \sum X_i}{n}, \quad (6)$$

$$a_1 = \frac{n \sum (X_i Y_i) - \sum X_i \sum Y_i}{n \sum X_i^2 - \sum X_i \sum X_i}, \quad (7)$$

Based on the data in Table 1, we could figure out the parameters a_0 and a_1 . The line equation could be expressed as

$$y_i = 5.50961 - 0.00662x, \quad (8)$$

The measuring model obtained based on LSM is shown in Figure 5. The black spots are the original measured data, and the red line is the fitted curve. The residual sum of squares was 0.09154 and the adj. R-Square was 0.91421.

4.2. Improved BP Neural Network

BP neural network is a supervised learning algorithm which is trained by the error back propagation algorithm. It is widely utilized due to its perfect theoretical system, clear algorithm flow and powerful function of data recognition and simulation compared to other evaluation methods [27–30]. BP neural network consisted of three layers including input layer, hidden layer, and output layer as shown in Figure 6. In this model, a series of motor frequencies formed the inputs and the corresponding outputs were the mean ceramic diameter.

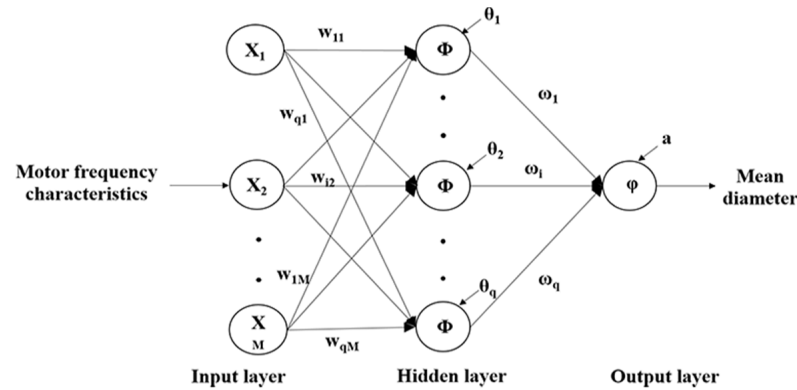


Figure 6. Topological structure of BP neural network model.

The input of the hidden layer was as follows.

$$u_i = \sum_{j=1}^M (w_{ij}x_j) + \theta_i, \tag{9}$$

where u_i was the input of the hidden layer, w_{ij} and θ_i were the connection weight and threshold between input layer and hidden layer where $i = 1, 2, \dots, q$ and $j = 1, 2, \dots, M$, respectively.

The output of the hidden layer was as follows.

$$y_i = \phi(u_i), \tag{10}$$

where y_i was the output of the hidden layer and ϕ was the transfer function of the hidden layer.

The input of the output layer could be expressed as follows.

$$v = \sum_{i=1}^q (\omega_i y_i) + a, \tag{11}$$

where v is the input of the output layer, ω_i was the weight of the output layer to the corresponding hidden layer, a was the threshold of the output layer.

Therefore, the output of the output layer was calculated as follows:

$$o = \varphi(v) = \varphi \left\{ \sum_{i=1}^q \omega_i \phi \left[\sum_{j=1}^M (w_{ij}x_j) + \theta_i \right] + a \right\}, \tag{12}$$

where o was the output of the output layer and φ was the transfer function of the output layer.

However, BP neural network also had its shortcomings as it sometimes fell into a local anomaly. It could not be guaranteed to converge to a global minimum. In addition, the BP algorithm took many training times, but the learning result was not satisfying. PSO was one of the optimization techniques and modern heuristic algorithms. It was found to be robust in solving nondifferentiability and nonlinearity problems which was applied for solving complex problems within stable convergence property and shorter computing time [31–33]. PSO first initialized a set of particles, and each particle represented a potential optimal solution in the search space. Each particle was treated as a volumeless particle with three indicators: location, velocity, and fitness value. Each particle kept track of its

coordinates and adjusted the current position through calculating the fitness value between the personal and group best. The value was dynamically adjusted according to its own flying experience. The algorithm flow of PSO is shown in Figure 7.

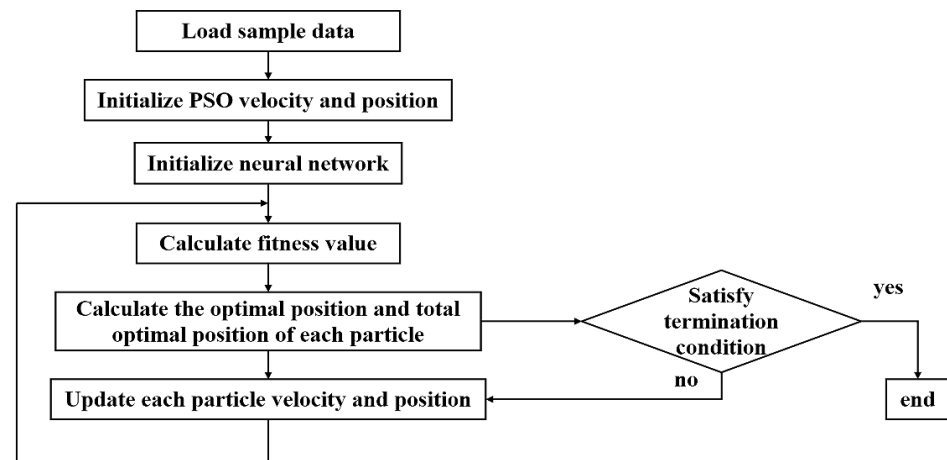


Figure 7. Algorithm flow of PSO neural network.

The data in Table 1 were used as the training sample and BP neural network based on PSO algorithm was achieved. The maximum number of iterations and the number of particles swarm was set to 800, the maximum training times of BP neural network was 200,000, the iterative weight and the accuracy were 0.035 and 0.004, respectively. The calculated model based on PSO-BP neural network was indicated in Figure 8. Results of comparison of Figures 5 and 8 indicate that the measuring model based on PSO-BP neural network was obviously better than that of LSM.

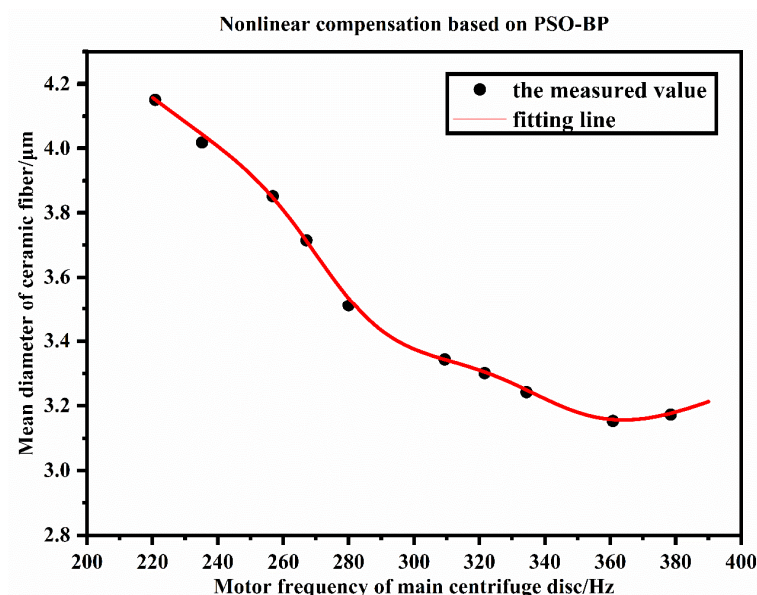


Figure 8. Nonlinear compensation model based on improved PSO-BP.

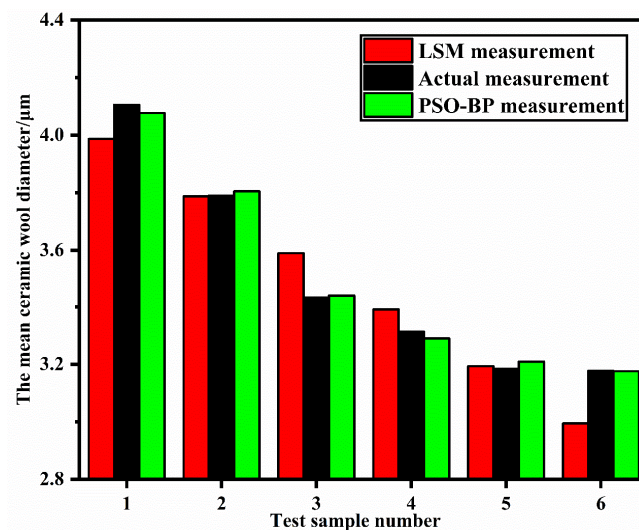
5. Practical Examination and Error Analysis

This paper finally selected another 6 samples for the actual testing and the measurement results were compared with those of two above-mentioned models to prove the accuracy of calculation model. The tested motor frequency ranged from 230 to 380 Hz with an adjacent interval of 30 Hz and all of the data are shown in Table 2. The measuring precision was calculated by the ratio of the difference between the measurement value and actual value.

Table 2. Results comparison between LSM and PSO-BP model.

Test Sample Number	Actual Mean Fiber Diameter/ μm	LSM Measuring Results/ μm	LSM Measuring Precision/%	PSO-BP Measuring Results/ μm	PSO-BP Measuring Precision/%
220.9	4.154	4.158	4.135	4.152	4.156
235.2	4.023	4.025	3.994	4.031	4.024
256.8	3.851	3.859	3.812	3.867	3.869
267.1	3.731	3.719	3.687	3.721	3.716
280.0	3.524	3.519	3.489	3.513	3.511
309.4	3.347	3.345	3.337	3.342	3.343
321.6	3.309	3.313	3.267	3.305	3.310
334.4	3.252	3.245	3.226	3.243	3.245
360.8	3.158	3.156	3.148	3.152	3.15
378.5	3.176	3.181	3.160	3.172	3.174

The predicted mean fiber diameters were compared with the measured mean values as indicated in Figure 9. Clearly; some error still existed between the measurement and the actual values. In the LSM model; the ceramic wool diameters decreased monotonously with the increasing main motor frequency. However; the vibration of the rotating disc made the fiber forming environment much more complex at the higher motor frequency. The actual results indicated that the diameter of the fiber hardly changed when the main motor frequency increased from 350 Hz to 380 Hz. At this point; the measuring precision of PSO-BP neural network was -0.045% while it was -5.760% for LSM. For the practical examination; the mean measurement error of PSO-BP and LSM was 0.471% and 2.656% , respectively. Its measuring accuracy was ideally situated for forecasting the ceramic wool diameter date timely using main motor frequency.

**Figure 9.** Comparison of measured and model predicted value.

6. Conclusions

- (1) The measurement of fiber mean diameter was a very important issue. Theory analysis, simulation analysis, and experiment were used to form a better understanding of the nonlinear problem between motor frequency and fiber mean diameter. The approximate simulation of the fiber formation was discussed, and improved BP neural network based on PSO algorithm was developed to predict the ceramic mean diameter successfully.
- (2) A great relationship between the main motor frequency and the ceramic mean diameter was built which had been verified by practical examination. Compared to the nonlinear compensation model based on LSM, the mean measurement error

of PSO-BP was 0.471% which was lower than that of LSM. The presented PSO-BP method was very valuable for predicting the wool diameter.

- (3) The neural networks could solve nonlinear problems successfully which was certified by the actual prediction of ceramic wool diameter. This shows a bright future in the subsequent wool production.

Author Contributions: Conceptualization, T.X.; methodology, T.X.; software, J.H.; validation, T.X., J.H., Y.L. and T.C.; formal analysis, T.X.; investigation, T.X.; resources, T.X.; data curation, J.H.; writing—original draft preparation, T.X.; writing—review and editing, J.H.; visualization, Y.L.; supervision, T.C.; project administration, T.X.; funding acquisition, T.X. All authors have read and agreed to the published version of the manuscript.

Funding: This research was funded by the Basic Science (Natural Science) Research Project of Higher Education of Jiangsu, grant number: 20KJB560008 and the Introduced Talent Research Fund Project of Nanjing Vocational University of Industry Technology, grant number: 101050618YK306.

Institutional Review Board Statement: Ethical review and approval were waived for this study due to this study not involving humans or animals.

Informed Consent Statement: Not applicable, for the study not involving humans.

Conflicts of Interest: The authors declare no conflict of interest.

References

1. Chen, Z.; Chen, Z.; Yang, Z.; Hu, J.; Yang, Y.; Chang, L.; Lee, L.J.; Xu, T. Preparation and characterization of vacuum insulation panels with super-stratified glass fiber core material. *Energy* **2015**, *93*, 945–954. [\[CrossRef\]](#)
2. Chu, S.; Majumdar, A. Opportunities and challenges for a sustainable energy future. *Nature* **2012**, *488*, 294–303. [\[CrossRef\]](#) [\[PubMed\]](#)
3. Wang, S.; Feng, Y.; Huang, Y.; Wu, J.; Ye, Y. A new method of rapid quality detection of vacuum insulation panels. *Sci. China Technol. Sci.* **2014**, *57*, 1602–1609. [\[CrossRef\]](#)
4. Xiao, Y.; Liu, Y.; Li, Y. Status and development of mineral wool made from molten blast furnace slag. *Baosteel Tech. Res.* **2011**, *5*, 3–8.
5. Barati, M.; Esfahani, S.; Utigard, T. Energy recovery from high temperature slags. *Energy* **2011**, *36*, 5440–5449. [\[CrossRef\]](#)
6. Li, L.; Xu, C.; Chang, R.; Yang, C.; Jia, C.; Wang, L.; Song, J.; Li, Z.; Zhang, F.; Fang, B.; et al. Thermal-responsive, super-strong, ultrathin firewalls for quenching thermal runaway in high-energy battery modules. *Energy Storage Mater.* **2021**, *40*, 329–336. [\[CrossRef\]](#)
7. Li, L.; Fang, B.; Ren, D.; Fu, L.; Zhou, Y.; Yang, C.; Zhang, F.; Feng, X.; Wang, L.; He, X.; et al. Thermal-Switchable, Trifunctional Ceramic-Hydrogel Nanocomposites Enable Full-Lifecycle Security in Practical Battery Systems. *ACS Nano* **2022**, *16*, 10729–10741. [\[CrossRef\]](#)
8. Li, B.B.; Chen, Z.F.; Chen, Z.; Qiu, J.; Zhou, Y.Q.; Zhou, J.M. Effect of vitreous fluid temperature on fiber diameter and surface topography of glass wool by centrifugal-spinneret-blow process. *Adv. Mater. Res.* **2012**, *415–417*, 1996–2001. [\[CrossRef\]](#)
9. Clauss, B.; Schawaller, D. Modern aspects of ceramic fiber development. *Adv. Sci. Technol.* **2006**, *50*, 1–8.
10. Ye, X.; Chen, Z.; Zhang, J.; Zhang, P. Two-layer separation technology of melt-spinning ceramic wool. *Mater. Res. Express* **2018**, *5*, 115201. [\[CrossRef\]](#)
11. Li, L.; Jia, C.; Liu, Y.; Fang, B.; Zhu, W.; Li, X.; Schaefer, L.A.; Li, Z.; Zhang, F.; Feng, X.; et al. Nanograin-glass dual-phasic, elasto-flexible, fatigue-tolerant, and heat-insulating ceramic sponges at large scales. *Mater. Today* **2022**, *54*, 72–82. [\[CrossRef\]](#)
12. Zhang, H.; Wang, H.; Zhu, X.; Qiu, Y.-J.; Li, K.; Chen, R.; Liao, Q. A review of waste heat recovery technologies towards molten slag in steel industry. *Appl. Energy* **2013**, *112*, 956–966. [\[CrossRef\]](#)
13. Zhao, D.; Zhang, Z.; Tang, X.; Liu, L.; Wang, X. Preparation of Slag Wool by Integrated Waste-Heat Recovery and Resource Recycling of Molten Blast Furnace Slags: From Fundamental to Industrial Application. *Energies* **2014**, *7*, 3121–3135. [\[CrossRef\]](#)
14. Abtahi, S.M.; Sheikhzadeh, M.; Hejazi, S.M. Fiber-reinforced asphalt-concrete—A review. *Constr. Build. Mater.* **2010**, *24*, 871–877. [\[CrossRef\]](#)
15. Zhao, D.; Zhang, Z.; Liu, L.; Wang, X. A Novel Kinematic Model for Molten Slag Fiberization: Prediction of Slag Fiber Properties. *Met. Mater. Trans. A* **2014**, *46*, 993–1001. [\[CrossRef\]](#)
16. Bajcar, T.; Blagojević, B.; Širok, B.; Dular, M. Influence of flow properties on a structure of a mineral wool primary layer. *Exp. Therm. Fluid Sci.* **2007**, *32*, 440–449. [\[CrossRef\]](#)
17. Gerogiorgis, D.; Pantias, D.; Paspaliaris, I. Stochastic modeling and simulation of fiber evolution during melt-blowing slag fiberization. In Proceedings of the Collected Proceedings of the TMS 2012 Annual Meeting (CD), TMS, Warrendale, PA, USA, 11–15 March 2012.

18. Chelikani, S.; Sparrow, E.M. Numerical Simulations of Plane-Wall Coanda Effects for Control of Fiber Trajectories in the Melt-Blown Process. *Ind. Eng. Chem. Res.* **2013**, *52*, 11639–11645. [[CrossRef](#)]
19. Blagojevic, B.; Širok, B.; Hočevnar, M. Monitoring and Control of Quality of the Primary Layer of Mineral Wool on a Disc Spinning Machine. *Instrum. Sci. Technol.* **2003**, *31*, 63–75. [[CrossRef](#)]
20. Sungkhaphaitoon, P.; Plookphol, T.; Wisutmethangoon, S. Centrifugal Atomization of Zinc Metal Powder for Friction Materials Application. *Adv. Mater. Res.* **2012**, *488–489*, 281–285. [[CrossRef](#)]
21. Mencinger, J.; Bizjan, B.; Širok, B. Numerical simulation of ligament-growth on a spinning wheel. *Int. J. Multiph. Flow* **2015**, *77*, 90–103. [[CrossRef](#)]
22. Bizjan, B.; Širok, B.; Govekar, E. Nonlinear Analysis of Mineral Wool Fiberization Process. *J. Comput. Nonlinear Dyn.* **2015**, *10*, 021005. [[CrossRef](#)]
23. Vad, J.; Morlin, B. Fluid Mechanical Model for Formation of Mineral Wool Fibers Applied in Polymer Composites. *Mater. Sci. Forum* **2007**, *537–538*, 269–276. [[CrossRef](#)]
24. Shinjo, J.; Umemura, A. Simulation of liquid jet primary breakup: Dynamics of ligament and droplet formation. *Int. J. Multiph. Flow* **2010**, *36*, 513–532. [[CrossRef](#)]
25. Qin, Y.; Lv, X.; Bai, C.; Pan, C.; Guibao, Q.; Jie, Z. Mechanism of Dry Molten Slag Granulation Using a Rotating Multi-Nozzle Cup Atomizer. *Steel Res. Int.* **2014**, *85*, 44–52.
26. Hagiwara, A.; Hobara, N.; Takizawa, K.; Sato, K.; Abe, H.; Naito, M. Microstructure control of SOFC cathodes using the self-organizing behavior of LSM/ScSZ composite powder material prepared by spray pyrolysis. *Solid State Ion.* **2007**, *178*, 1123–1134. [[CrossRef](#)]
27. Ma, D.; Zhou, T.; Chen, J.; Qi, S.; Shahzad, M.A.; Xiao, Z. Supercritical water heat transfer coefficient prediction analysis based on BP neural network. *Nucl. Eng. Des.* **2017**, *320*, 400–408. [[CrossRef](#)]
28. Huang, L.; Huang, J.; Wang, W. The Sustainable Development Assessment of Reservoir Resettlement Based on a BP Neural Network. *Int. J. Environ. Res. Public Health* **2018**, *15*, 146. [[CrossRef](#)]
29. Guo, Y.; Zhao, Z.; Huang, L. SoC Estimation of Lithium Battery Based on Improved BP Neural Network. *Energy Procedia* **2017**, *105*, 4153–4158. [[CrossRef](#)]
30. Geng, X.; Lu, S.; Jiang, M.; Sui, Q.; Lv, S.; Xiao, H.; Jia, Y.; Jia, L. Research on FBG-Based CFRP Structural Damage Identification Using BP Neural Network. *Photon Sens.* **2018**, *8*, 168–175. [[CrossRef](#)]
31. Eberhart, R.C.; Shi, Y. Comparison between genetic algorithms and particle swarm optimization. In Proceedings of the Evolutionary Programming VII, 7th International Conference, EP98, San Diego, CA, USA, 25–27 March 1998; Springer: Berlin/Heidelberg, Germany, 1998.
32. Zeng, X.G. A Particle Swarm Optimization Approach for Optimum Design of PID Controller. *Mach. Des. Manuf.* **2007**, *19*, 384–391.
33. Xia, R.; Huang, J.; Chen, Y.; Feng, Y. A study of the method of the thermal conductivity measurement for VIPs with improved RBF neural networks. *Measurement* **2016**, *87*, 246–254. [[CrossRef](#)]

Disclaimer/Publisher’s Note: The statements, opinions and data contained in all publications are solely those of the individual author(s) and contributor(s) and not of MDPI and/or the editor(s). MDPI and/or the editor(s) disclaim responsibility for any injury to people or property resulting from any ideas, methods, instructions or products referred to in the content.